

Range ambiguity suppression under high-resolution estimation using the MUSIC-AP algorithm for pulse-Doppler radar[☆]

Yuanshuai Li^a, Shaoqiang Chang^{a,c}, Zihao Liu^a, Wei Ren^b, Quanhua Liu^{a,c,*}

^a The Key Laboratory of Electronic and Information Technology in Satellite Navigation, Ministry of Education, Beijing Institute of Technology, Beijing 100081, China

^b The Department of Computing, The Hong Kong Polytechnic University, Hong Kong

^c The Beijing Institute of Technology Chongqing Innovation Center, Chongqing, 401120, China

ARTICLE INFO

Keywords:

Alternating projection
High-resolution estimation
Multiple-signal classification
Range ambiguity suppression
Waveform diversity

ABSTRACT

Range ambiguity is a significant challenge in conventional pulse-Doppler radar systems with medium or high pulse repetition frequencies, greatly impacting radar detection and imaging capabilities. The classic approaches such as waveform diversity and compressed sensing are based on the isolation between pulses. However, these methods encounter issues like residual ambiguity and grid mismatch, resulting in poor range ambiguity suppression performance. In this paper, the multiple signal classification-alternating projection (MUSIC-AP) method is proposed to address these challenges and achieve high-resolution estimation. The proposed method converts the range-velocity estimate into a spectrum estimate, enabling the utilization of the MUSIC algorithm to solve the grid mismatch problem and improve echo reconstruction. Then, to mitigate the effect of ambiguous energy on reconstruction, the MUSIC reconstruction subprocess is embedded into the AP framework. Through iterative approximation, the method gradually suppresses ambiguous and noise energy, thereby further enhancing the echo reconstruction accuracy and range ambiguity suppression performance. Simulations demonstrate the effectiveness of the proposed method. Moreover, algorithm analysis is conducted, considering aspects such as resolution, robustness, and sparsity, which provides a basis for parameter selection and applicability conditions.

1. Introduction

Pulse-Doppler (PD) technology has been widely applied in radar systems to detect and track moving targets in harsh environments [1]. Conventional PD radars transmit coherent pulses with constant pulse width and pulse repetition frequency (PRF) within the coherent processing interval (CPI). It can effectively improve the target signal-to-noise ratio (SNR) by performing matched filtering and PD processing. However, with constant modulation parameters, echoes appear periodically along the range dimension and velocity dimension, resulting in range ambiguity and velocity ambiguity [2–4]. A high PRF is usually used in search and track mode to obtain a large range of unambiguous velocity. However, severe range ambiguity has a great impact on radar target detection and imaging.

Several techniques for mitigating range ambiguity have been proposed over the years. The first approach involves transmitting several

groups of coherent signals with different PRFs [5–8]. The Chinese remainder theorem has been utilized to resolve ambiguity and obtain the true range of target. However, this method cannot effectively utilize echo energy, and ghost images or false targets may emerge when there are multiple targets.

The second approach involves using the range-gating characteristics of waveform diversity [9–11] to transmit different modulated pulses. The ambiguity is resolved by constructing receiving filter banks in different range segments. Common methods of waveform diversity include interpulse phase agility [12–14]. In this method, the phase coherence of the slow-time dimensional ambiguous signal is destroyed, causing the ambiguous energy to disperse in the Doppler dimension. However, this method depends on phase changes, which are very sensitive to noise and can raise the Doppler dimension sidelobe level as a whole. Another method, interpulse frequency agility [15–20], modulates each

[☆] This work was supported in part by the Beijing Institute of Technology Research Fund Program for Young Scholars, China under Grant XSQD202205012, and in part by the Natural Science Foundation of Chongqing, China under Grant cstc2020jcyj-msxmX0260.

* Corresponding author at: The Key Laboratory of Electronic and Information Technology in Satellite Navigation, Ministry of Education, Beijing Institute of Technology, Beijing 100081, China.

E-mail addresses: yuanshuaili_bit@163.com (Y. Li), shaoqiangchang@bit.edu.cn (S. Chang), zhliubit@bit.edu.cn (Z. Liu), wei-2022.ren@polyu.edu.hk (W. Ren), liuquanhua@bit.edu.cn (Q. Liu).

<https://doi.org/10.1016/j.sigpro.2023.109237>

Received 5 June 2023; Received in revised form 18 July 2023; Accepted 28 August 2023

Available online 1 September 2023

0165-1684/© 2023 Elsevier B.V. All rights reserved.

Table 1
Several schemes to solve the problem of range ambiguity.

Schemes	Properties	Limitations
Multi-PRFs	Resolves ambiguity by the Chinese remainder theorem	Increases the total search time, and ghosts or false targets may occur when multiple targets are present
Waveform diversity	The ambiguous energy is dispersed by the isolation between signals	The RSM effect is produced and the occlusion problem of short-range strong ambiguous energy cannot be solved
Compressive sensing	The echo of each range segment is reconstructed by atomic correlation to realize ambiguity suppression	Grid mismatch leads to straddling loss and signal distortion, which reduces the reconstruction accuracy and ambiguity suppression performance

pulse with a different carrier frequency, preventing ambiguous signals from being coherently integrated in the fast-time dimension. However, bandwidth synthesis is conducted through multiframe joint processing, which reduces the maximum unambiguous velocity. In the interpulse code agility approach [21–25], different pulses modulate different coding sequences at the same carrier frequency, so it does not decrease the maximum unambiguous velocity. Nevertheless, different pulses produce various range sidelobe structures, and this phenomenon is known as the range sidelobe modulation (RSM) effect [26–28]. During PD processing, the sidelobe energy spreads along the Doppler dimension, obscuring small targets that are close to larger targets. Although the waveform diversity PD radar system achieves range-gating, ambiguous energy is not removed but rather distributed on the range-Doppler plane as dispersed energy. The cross-correlation of short-range strong ambiguous echoes is still likely to be stronger than the autocorrelation of long-range weak targets, severely affecting the detection of the desired targets.

The third method involves the use of compressive sensing [29–31]. In [32], an unambiguous delay-Doppler recovery method for random phase-coded pulses based on compressive sensing is discussed. The approach suppresses range ambiguity by estimating the scattering information and reconstructing the echo of various range segments. However, this method places a strong requirement on the sparsity of the scene and requires relatively high computational resources. The size of the sensing matrix is proportional to the pulse repetition time (PRT), and the estimation of delay-Doppler is a discrete grid value. Grid mismatch can lead to potential issues such as straddling loss and imaging distortion [33]. Generally, decreasing the grid spacing can reduce the estimation error. However, determining the ideal grid spacing is challenging, and refining the grid significantly increases the calculational burden and atomic correlations. Table 1 provides a summary of the aforementioned methods. Despite their benefits, the above schemes have certain limitations, and solving the range ambiguity in PD radar remains a significant challenge. In addition to these, there are numerous new radar systems aimed at mitigating range ambiguity [34], such as frequency-diverse arrays, which hold vast potential for application and further development.

Our aim is to solve the grid mismatch to obtain high-resolution estimation. This in turn improves the reconstruction performance and range ambiguity suppression performance. Recently, researchers have introduced the concept of atomic norm [35–39] to describe signal characteristics in a continuous parameter space, preventing grid mismatch. Convex optimization [40] is used to obtain continuous estimated values of the desired information. However, its low calculational efficiency makes it challenging to apply to large-dimensional data, and high scene sparsity is required. According to [41,42], the MUSIC algorithm is highly stable and has low computational complexity for reconstructing well-separated frequencies. Furthermore, it can recover arbitrarily closely spaced frequencies as long as the noise is sufficiently small.

The motivation, solution and outcomes of this paper are depicted in Fig. 1. This paper proposes a novel method called the MUSIC-AP algorithm, which comprehensively considers the computational complexity, high-resolution estimation, and ambiguity suppression. Inspired by the MUSIC algorithm in direction of arrival estimation, this paper employs the MUSIC algorithm to solve the grid mismatch problem. However, some preprocessing is required to make the MUSIC high-resolution estimation algorithm applicable to scenarios where the radar transmits agile pulses with range ambiguity. Then, the AP algorithm [43,44] is adopted to obtain the next iteration point by performing orthogonal projection on a closed convex set to reduce the effect of dispersed ambiguous energy. The MUSIC-AP algorithm overcomes the resolution limitation of conventional radar, and effectively prevents grid mismatch thereby improving the reconstruction effect and range ambiguity suppression.

In summary, the contributions of the proposed method are:

1. The range-velocity estimation problem is converted into a spectral estimation problem so that the MUSIC algorithm is applicable;
2. High-resolution estimation is performed with the MUSIC algorithm based on the Hankel matrix, combined with the least square (LS) method to realize internal echo reconstruction at different range segments in range ambiguity scenes;
3. The MUSIC reconstruction subprocess is embedded into the AP outer framework to gradually suppress the ambiguous energy in nonlocal range segments and noise energy, which further improves the echo reconstruction accuracy and range ambiguity suppression performance.

The rest of the paper is organized as follows: Section 2 constructs the line spectrum estimation model in the waveform agility system without range ambiguity, and introduces the MUSIC algorithm for high-resolution estimation. Section 3 describes the line spectrum estimation model in the waveform agility system with range ambiguity, and introduces the MUSIC-AP algorithm range ambiguity suppression under high-resolution estimation. Section 4 demonstrates the effectiveness and feasibility of the proposed algorithm through simulations, and analyzes the resolution, robustness, and sparsity of the algorithm. Section 5 concludes the paper.

2. High-resolution estimation

In this section, the range-velocity estimation problem in PD radar that transmits agile waveforms is converted into a spectral estimation problem by temporarily disregarding the range ambiguity, and a line spectrum estimation model is constructed to achieve high-resolution estimation using the MUSIC algorithm based on the Hankel matrix. Echo models in the frequency domain and time domain are derived to realize echo reconstruction.

2.1. Line spectrum estimation model without range ambiguity

We assume that radar transmits the phase-coded signal and there are N_{prt} different pulse sequences in a CPI. Each pulse $u_n(n = 0, 1, \dots, N_{prt} - 1)$ is modulated by a different phase code sequence with M chips. The time domain of the baseband signal of the n th transmission pulse can be represented as

$$u_n(t) = \frac{1}{\sqrt{M}} \sum_{m=0}^{M-1} c_{n,m} \text{rect} \left(\frac{t - mT_c - nT_r}{T_c} \right) \quad (1)$$

$$\text{rect} \left(\frac{t}{T_c} \right) = \frac{1}{\sqrt{T_c}} \begin{cases} 1 & 0 \leq t \leq T_c \\ 0 & \text{otherwise} \end{cases} \quad (2)$$

where $c_{n,m} = e^{j\phi_n(m)}$ is the m th phase code in the n th pulse, and $\phi_n(m)$ is the phase modulation function, which can take any value in the

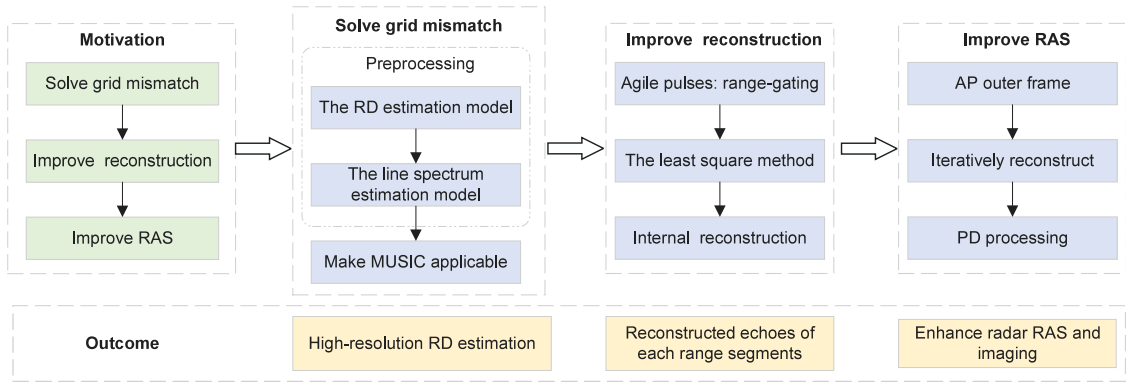


Fig. 1. Graphical abstract of the work in this article. MUSIC, RAS, RD, and AP represent multiple-signal classification, range ambiguity suppression, range-Doppler, and alternating projection respectively.

interval $[0, 2\pi)$. t , T_c and T_r denote the fast-time, the chip width and pulse repetition interval (PRI), respectively.

The n th transmission pulse frequency domain can be represented as

$$U_n(f) = \sqrt{\frac{T_c}{M}} \text{sinc}(\pi f T_c) e^{j\pi f T_c} \sum_{m=0}^{M-1} c_{n,m} e^{-j2\pi f m T_c} \quad (3)$$

where f denotes the fast-time frequency.

The radar echoes can be approximated as the superposition of the subechoes produced by multiple scattering points. Assuming there are K targets, τ_k^n and v_k^n are the time delay and Doppler shift of the k th target during the n th PRI, respectively. If the echo broadening and compression are ignored, the n th received signal after frequency conversion under the baseband can be represented as

$$r_n(t) = \sum_{k=1}^K \sigma_k e^{-j2\pi f_c \tau_k^n} u_n(t - \tau_k^n) e^{j2\pi v_k^n t} \quad (4)$$

where σ_k is the complex backscatter coefficient of the k th target, supposing it is constant in a CPI. f_c denotes the carrier frequency of the radar. At this moment, if the conventional PD processing is used, the echo is first processed by a matched filter bank corresponding to the range segment in the fast-time domain, and then the fast Fourier transform (FFT) is performed in the slow-time domain to achieve two-dimensional coherent accumulation of echo energy in each range segment. The difference is that the proposed method converts the echo data into the line spectrum data for subsequent processing.

We assume that the phase shift caused by the Doppler frequency shift within the pulse width can be ignored and that the target velocity is constant within the CPI, i.e., $v_k^n \approx v_k$. The received signal at the n th PRT can be represented as

$$r_n(t) = \sum_{k=1}^K \sigma_k e^{-j2\pi f_c \tau_k^n} u_n(t - \tau_k^n) e^{j2\pi v_k^n T_r} \quad (5)$$

Then, (5) can be transformed into the following through the Fourier transformation.

$$R_n(f) = \sum_{k=1}^K \sigma_k U_n(f) e^{-j2\pi f_c \tau_k^n} e^{j2\pi v_k^n T_r} e^{-j2\pi f \tau_k^n} \quad (6)$$

Since the velocity of the target is much smaller than the velocity of light, it can be assumed that the change of the target delay between pulses can be ignored, that is, $\tau_k^n \approx \tau_k$. The above equation can be simplified as

$$R_n(f) = U_n(f) \sum_{k=1}^K \sigma_k e^{-j2\pi f_c \tau_k} e^{j2\pi v_k T_r} e^{-j2\pi f \tau_k} \quad (7)$$

Then, (7) can be discretized as

$$R_n(l) = U_n(l \Delta f) \sum_{k=1}^K \beta_k e^{j2\pi v_k T_r} e^{-j2\pi l \Delta f \tau_k}$$

$$l = 0, 1, 2, \dots, N_{spe} - 1 \quad (8)$$

$$n = 0, 1, 2, \dots, N_{prt} - 1$$

where $\beta_k = \sigma_k e^{-j2\pi f_c \tau_k}$ and $f = l \Delta f$, $\Delta f = f_s / N_{spe}$ is the frequency interval, f_s is the sampling rate, and N_{spe} is the number of spectrum points. The unambiguous echo spectrum matrix in CPI can be represented as

$$\mathbf{R}(f) = \begin{bmatrix} R_{0,0} & R_{1,0} & \dots & R_{N_{prt}-1,0} \\ R_{0,1} & R_{1,1} & \dots & R_{N_{prt}-1,1} \\ \vdots & \vdots & \ddots & \vdots \\ R_{0,N_{spe}-1} & R_{1,N_{spe}-1} & \dots & R_{N_{prt}-1,N_{spe}-1} \end{bmatrix} \quad (9)$$

Eq. (9) is a two-dimensional (2D) line spectrum estimation model, and $\mathbf{R}(f) \in \mathbb{C}^{N_{spe} \times N_{prt}}$ is a linear combination of K -2D complex sinusoidal signals, which can be represented as

$$\mathbf{R}(f) = \sum_{k=1}^K \beta_k \mathbf{a}_{N_{spe}}(\tau_k) \mathbf{b}_{N_{prt}}^H(v_k) \odot \mathbf{U}(f) \quad (10)$$

where $\mathbf{a}_{N_{spe}}(\tau)$, $\mathbf{b}_{N_{prt}}(v)$ and $\mathbf{U}(f)$ are expressed as

$$\mathbf{a}_{N_{spe}}(\tau) = [1, e^{-j2\pi \Delta f \tau}, \dots, e^{-j2\pi (N_{spe}-1) \Delta f \tau}]^T \quad (11)$$

$$\mathbf{b}_{N_{prt}}(v) = [1, e^{-j2\pi v T_r}, \dots, e^{-j2\pi (N_{prt}-1) v T_r}]^T \quad (12)$$

$$\mathbf{U}(f) = [U_0(f), U_1(f), \dots, U_{N_{prt}-1}(f)] \quad (13)$$

where T , H and \odot represent the transpose, conjugate transpose and Hadamard product, respectively. The steering vector matrix $\mathbf{A}_{N_{spe}}(\tau) \in \mathbb{C}^{N_{spe} \times K}$ and $\mathbf{B}_{N_{prt}}(v) \in \mathbb{C}^{N_{prt} \times K}$ can be defined as

$$\mathbf{A}_{N_{spe}}(\tau) = [\mathbf{a}_{N_{spe}}(\tau_1), \mathbf{a}_{N_{spe}}(\tau_2), \dots, \mathbf{a}_{N_{spe}}(\tau_K)] \quad (14)$$

$$\mathbf{B}_{N_{prt}}(v) = [\mathbf{b}_{N_{prt}}(v_1), \mathbf{b}_{N_{prt}}(v_2), \dots, \mathbf{b}_{N_{prt}}(v_K)] \quad (15)$$

Notably, some targets may have the same frequency in one dimension but not in another dimension, i.e., if $\tau_m = \tau_n$, $m \neq n$, then $v_m \neq v_n$ must be satisfied.

Then, (10) can be rewritten as matrix form.

$$\mathbf{R}(f) = \mathbf{A}_{N_{spe}}(\tau) \mathbf{B}_{N_{prt}}^H(v) \odot \mathbf{U}(f) \quad (16)$$

where $\mathbf{\beta} = \text{diag}(\beta_1, \beta_2, \dots, \beta_K) \in \mathbb{C}^{K \times K}$. The role of the $\text{diag}(\cdot)$ function is to construct a diagonal matrix. Based on the echo spectrum matrix obtained by (16), a corresponding weighted matched filter bank can be expressed as

$$\mathbf{H}(f) = \mathbf{U}(f)^* \odot [|\mathbf{U}(f)|^2]^{-1} \quad (17)$$

where $[\cdot]^{-1}$ denotes taking the reciprocal of each entry of the object, and $*$ denotes the conjugate operator. The joint mismatched filter bank

can also be constructed to ensure that the spectrum is coherent in the slow-time dimension. The first mismatched filter in (17) is used for subsequent processing. The echo power spectrum matrix is obtained as

$$\begin{aligned} \mathbf{Y}(f, t_r) &= \mathbf{R}(f) \odot \mathbf{H}(f) \\ &= \mathbf{A}_{N_{spe}}(\tau) \mathbf{B}_{N_{prt}}^H(\mathbf{v}) \\ &= \begin{bmatrix} y_0(f), & y_1(f), & \dots, & y_{N_{prt}-1}(f) \end{bmatrix} \\ &= \begin{bmatrix} x_0(t_r), & x_1(t_r), & \dots, & x_{N_{spe}-1}(t_r) \end{bmatrix}^T \end{aligned} \quad (18)$$

where $t_r = nT_r$, in which $n = 0, 1, \dots, N_{prt} - 1$ denotes the slow-time. The element in the n th column and the l th row of $\mathbf{Y}(f, t_r)$ is

$$\mathbf{Y}(l\Delta f, nT_r) = \sum_{k=1}^K \beta_k e^{j2\pi v_k n T_r} e^{-j2\pi l \Delta f \tau_k} \quad (19)$$

The n th column contains the power spectrum generated by the n th received echo using the corresponding weighted matched filter.

$$y_n(f) = R_n(f) \odot H_n(f) = \sum_{k=1}^K \beta_k e^{j2\pi v_k n T_r} e^{-j2\pi f \tau_k} \quad (20)$$

The l th row contains the phase change of the l th frequency unit in the slow-time dimension.

$$x_l(t_r) = \sum_{k=1}^K \beta_k e^{-j2\pi l \Delta f \tau_k} e^{j2\pi v_k t_r} \quad (21)$$

To reduce the influence of noise and improve the estimation accuracy, the FFT is then performed in the slow-time dimension to achieve coherent accumulation. Window functions can be used to reduce spectral leakage. For the convenience of derivation, zero padding and windowing are not used.

$$\begin{aligned} \mathbf{S}(f, v) &= \text{FFT}\{\mathbf{Y}(f, t_r), t_r\} \\ &= \left[\text{FFT}\{x_0(t_r)\}, \text{FFT}\{x_1(t_r)\}, \dots, \text{FFT}\{x_{N_{spe}-1}(t_r)\} \right]^T \end{aligned} \quad (22)$$

where $\text{FFT}\{x_l(t_r)\}$ is represented as

$$\text{FFT}\{x_l(t_r)\} = \sum_{k=1}^K \beta_k e^{-j2\pi l \Delta f \tau_k} \text{FFT}\{e^{j2\pi v_k t_r}\} = \sum_{k=1}^K \beta_k e^{-j2\pi l \Delta f \tau_k} \delta(v - v_k) \quad (23)$$

in which $\delta(\cdot)$ is the Dirac function. Therefore, when $v = v_k$, the coherently accumulated single-snapshot peak data can be obtained.

$$\mathbf{S}(f, v_k) = \sum_{k=1}^{K_{v_k}} \beta_k \delta(0) e^{-j2\pi f \tau_k} \quad (24)$$

where K_{v_k} represents the number of targets with Doppler frequency v_k . The conjugate and discretization representation of (24) is

$$\mathbf{S}^*(l, v_k) = \sum_{k=1}^{K_{v_k}} (\beta_k \delta(0))^* e^{j2\pi l \Delta f \tau_k} = \sum_{k=1}^{K_{v_k}} s_k e^{j2\pi l f_k} \quad (25)$$

Eq. (25) is the superposition of multiple complex sinusoidal signals. Thus, the estimation of scattering points can be converted into line spectrum estimation. Specifically, the frequency components satisfy the following equation.

$$f_k = \tau_k \Delta f = \frac{\tau_k f_s}{N_{spe}} \quad (26)$$

Hence, the construction of the line spectrum estimation model in the scenario without range ambiguity is completed. In the following subsection, we will derive the methodology for obtaining frequency estimation. By utilizing Eq. (26), the delay estimation can be derived from the frequency estimation.

2.2. High-resolution estimation based on MUSIC

In this subsection, different from the MUSIC algorithm in direction of arrival estimation, range-Doppler high-resolution estimation is implemented by applying the MUSIC algorithm to the abovementioned line spectrum model. Then combined with the least square method to realize the echo reconstruction.

To facilitate representation, the data in (25) can be equivalently represented as

$$y_n = \sum_{k=1}^K s_k e^{j2\pi f_k n} \quad (27)$$

The Hankel matrix can be constructed based on the signal in (27)

$$\mathbf{H}(y) = \begin{bmatrix} y_1 & y_2 & \dots & y_n \\ y_2 & y_3 & \dots & y_{n+1} \\ \vdots & \vdots & \ddots & \vdots \\ y_m & y_{m+1} & \dots & y_N \end{bmatrix} \quad (28)$$

where $m + n = N + 1$. $\mathbf{H}(y)$ can be represented as

$$\mathbf{H}(y) = \sum_{k=1}^K s_k \begin{bmatrix} 1 \\ e^{j2\pi f_k} \\ \vdots \\ e^{j2\pi(m-1)f_k} \end{bmatrix} [1, e^{j2\pi f_k}, \dots, e^{j2\pi(n-1)f_k}] \quad (29)$$

$$\mathbf{H}(y) = \Phi^m \mathbf{S} (\Phi^n)^T \quad (30)$$

$$\mathbf{S} = \text{diag}(s_1, s_2, \dots, s_K) \quad (31)$$

where Φ^m is the Vandermonde matrix.

$$\begin{aligned} \Phi^m &= \begin{bmatrix} 1 & 1 & \dots & 1 \\ e^{j2\pi f_1} & e^{j2\pi f_2} & \dots & e^{j2\pi f_K} \\ \vdots & \vdots & \ddots & \vdots \\ e^{j2\pi(m-1)f_1} & e^{j2\pi(m-1)f_2} & \dots & e^{j2\pi(m-1)f_K} \end{bmatrix} \\ &= [\Phi^m(f_1), \Phi^m(f_2), \dots, \Phi^m(f_K)] \end{aligned} \quad (32)$$

If $K \leq \min(m, n)$, then $\text{rank}(\mathbf{H}(y)) = K$. Φ^m is the signal subspace. Therefore, it is necessary to identify the orthogonal complement space of the signal subspace, i.e., the noise subspace, to estimate f_k in (26).

The singular value decomposition (SVD) of $\mathbf{H}(y)$ is as

$$\mathbf{H}(y) = [\mathbf{U}_1 \ \mathbf{U}_2] \begin{bmatrix} \Sigma_1 & 0 \\ 0 & 0 \end{bmatrix} [\mathbf{V}_1 \ \mathbf{V}_2]^* \quad (33)$$

where \mathbf{U}_1 and \mathbf{U}_2 are the signal subspace and the noise subspace, respectively. The frequency number K is determined by the second-order statistic of eigenvalues method [45]. Then, the eigenvectors of the $N-K$ smallest eigenvalues are the noise subspace.

The imaging function [42] can be represented as

$$\mathbf{J}(f) = \frac{\|\Phi^m(f)\|_2}{\|\mathbf{U}_2^H \Phi^m(f)\|_2} \quad (34)$$

We can improve the resolution by refining the frequency interval of $\Phi^m(f)$ and accurately recover all frequencies by determining the local maximum value of $\mathbf{J}(f)$. In the absence of noise, accurate estimation of all frequencies can be guaranteed only if the total quantity of measured data is at least twice the number of different frequencies to be recovered. If there is noise, robustness analysis will be performed later through simulation.

Upon obtaining \hat{f}_k , which is named as range frequency, the estimated delay $\hat{\tau}_k$ can be ascertained through (26). $\mathbf{A}_{N_{spe}}(\hat{\tau})$ can be computed by applying (14). Furthermore, the LS method can be combined with (18) to obtain the following data which contains Doppler frequency information.

$$[\hat{\mathbf{B}}_{N_{prt}}^H(\mathbf{v})] = (\mathbf{A}_{N_{spe}}(\hat{\tau}))^\dagger \cdot \mathbf{Y}(f, t_r) \quad (35)$$

where \dagger is a pseudo-inverse operator and $[\mathbf{B}\mathbf{B}_{N_{prt}}^H(v)]$ is the linear superposition of the Doppler-frequency complex sinusoidal signals. Then, the reconstructed echo spectrum can be obtained by

$$\hat{\mathbf{R}}(f) = \mathbf{A}_{N_{spe}}(\hat{\tau}) \cdot [\mathbf{B}\mathbf{B}_{N_{prt}}^H(v)] \odot [\mathbf{H}(f)]^{-1} \quad (36)$$

The Doppler frequency \hat{v}_k estimation can be accomplished through the aforementioned MUSIC algorithm to process the data containing Doppler frequency information in (35). Subsequently, (15) can be applied to obtain $\mathbf{B}_{N_{prt}}(\hat{v})$, and $\hat{\mathbf{b}}$ can be determined by

$$\hat{\mathbf{b}} = [\mathbf{B}\mathbf{B}_{N_{prt}}^H(v)] \cdot (\mathbf{B}_{N_{prt}}^H(\hat{v}))^\dagger \quad (37)$$

Thus far, we have completed the high-resolution estimation of scatterers and the reconstruction of the echo spectrum in an unambiguous scenario.

If the pulse truncation effect reaches a level that cannot be ignored, the above frequency domain echo model will be affected to a certain extent. We can reconstruct echo based on the time domain echo model. Assuming that the echo truncation length is equal to the pulse width T_p , the truncated echo is expressed as

$$\tilde{r}_n(t) = J_n(t) \sum_{k=1}^K \sigma_k e^{-j2\pi f_c \tau_k} u_n(t - \tau_k) e^{j2\pi v_k n T_r} \quad (38)$$

where $J_n(t)$ is the truncation function.

$$J_n(t) = \begin{cases} 1 & T_p + nT_r \leq t \leq (n+1)T_r \\ 0 & \text{otherwise} \end{cases} \quad (39)$$

First, the estimated delay $\hat{\tau}_k$ is used to construct the n th time-domain pulse echo of the k th target. If the estimated delay is not the grid delay point, the reconstructed time-domain echo is obtained by constructing the frequency domain echo and then inverse fast Fourier transform (IFFT) processing.

$$\hat{r}_{nk}(t) = e^{-j2\pi f_c \hat{\tau}_k} u_n(t - \hat{\tau}_k) \quad (40)$$

The time-domain echo matrix constructed from the K targets is as

$$\hat{\mathbf{r}}_n(t) = [\hat{r}_{n1}(t), \hat{r}_{n2}(t), \dots, \hat{r}_{nk}(t), \dots, \hat{r}_{nK}(t)] \quad (41)$$

$\hat{\mathbf{r}}_n(t)$ is discretized as $\hat{\mathbf{r}}_n \in \mathbb{C}^{N_r \times K}$, and $N_r = T_r f_s$ is the number of sampling points in the fast time domain of the echo. The truncation matrix $\mathbf{J} \in \mathbb{C}^{(N_r - N_p) \times N_r}$ is

$$\mathbf{J} = \begin{bmatrix} 0 & \dots & 0 & 1 & 0 & \dots & 0 \\ \vdots & \ddots & \vdots & 0 & 1 & \ddots & \vdots \\ \vdots & \vdots & \vdots & \vdots & \ddots & \ddots & 0 \\ 0 & \dots & 0 & 0 & \dots & 0 & 1 \end{bmatrix} \quad (42)$$

$\underbrace{\hspace{10em}}_{N_p} \quad \underbrace{\hspace{10em}}_{N_r - N_p}$

where $N_p = T_p f_s$ is the number of truncated points. According to the echo model in (38), the n th reconstructed truncated echo can be represented as

$$\hat{\mathbf{r}}_n = \mathbf{J} \cdot \hat{\mathbf{r}}_n \cdot \hat{\mathbf{c}}_n \quad (43)$$

Here, vector $\hat{\mathbf{c}}_n \in \mathbb{C}^{K \times 1}$ can be expressed as

$$\hat{\mathbf{c}}_n = [c_{n1}, c_{n2}, \dots, c_{nk}, \dots, c_{nK}]^T \quad (44)$$

where $c_{nk} = \sigma_k e^{j2\pi v_k n T_r}$ contains the complex amplitude (σ_k) and Doppler frequency modulation ($e^{j2\pi v_k n T_r}$) of the target. The LS method can be effectively employed to derive the vector $\hat{\mathbf{c}}_n$.

$$\hat{\mathbf{c}}_n = (\mathbf{J} \cdot \hat{\mathbf{r}}_n)^\dagger \cdot \tilde{\mathbf{r}}_n \quad (45)$$

where $\tilde{\mathbf{r}}_n$ is the n th true truncated echo discretization vector. Then, the n th reconstructed truncated echo can be obtained by the following equation.

$$\hat{\mathbf{r}}_n = \mathbf{J} \cdot \hat{\mathbf{r}}_n \cdot (\mathbf{J} \cdot \hat{\mathbf{r}}_n)^\dagger \cdot \tilde{\mathbf{r}}_n \quad (46)$$

After reconstructing the N_{prt} truncated echoes in a CPI, the matrix \mathbf{C} containing Doppler frequency information can be constructed.

$$\mathbf{C} = [\hat{\mathbf{c}}_0, \hat{\mathbf{c}}_1, \dots, \hat{\mathbf{c}}_{N_{prt}-1}] \quad (47)$$

Finally, processing the data from (47) using the aforementioned MUSIC algorithm yields the estimated Doppler frequency \hat{v}_k . High-resolution estimation of scatterers and time-domain echo reconstruction without range ambiguity are achieved. In the subsequent scenarios in this paper, we assume that there are no scattering points in the truncation area, so the pulse truncation effect can be ignored, and the frequency domain echo model is adopted to realize echo reconstruction.

3. Range ambiguity suppression

This section presents the construction of a line spectrum estimation model for range ambiguity in PD radar transmitting agile waveforms. The proposed MUSIC-AP algorithm is to combine the MUSIC algorithm with the AP scheme to achieve high-resolution estimation and enhance range ambiguity suppression.

3.1. Line spectrum estimation model with range ambiguity

In this subsection, an echo spectrum model of range ambiguity is constructed. The presence of echo folding in distinct range segments can severely degrade the imaging and detection performance, as a long-range weak target may be obstructed by the energy distribution of a short-range strong target.

With the assumption of P ambiguous range segments, the echo spectrum matrix of (16) is expanded as

$$\mathbf{R}(f) = \sum_{p=1}^P \mathbf{R}_p(f) = \sum_{p=1}^P \mathbf{A}_{p, N_{spe}}(\tau) \mathbf{b}_p \mathbf{B}_{p, N_{prt}}^H(v) \odot \mathbf{U}_p(f) \quad (48)$$

The echo spectrum matrix $\mathbf{R}_p(f)$, pertaining to the p th range segment, is defined identically to that of (16). The transmitted signal spectrum matrix of the p th range segment, denoted as $\mathbf{U}_p(f)$, is obtained by cyclically shifting $\mathbf{U}_1(f)$ as defined in Eq. (13), $p - 1$ PRTs toward the right along the column direction.

$$\mathbf{U}_p(f) = [\mathbf{U}_{N_{prt}-p+1}(f) \dots \mathbf{U}_{N_{prt}-1}(f), \mathbf{U}_0(f) \dots \mathbf{U}_{N_{prt}-p}(f)] \quad (49)$$

Range-gating is achieved by constructing a filter bank corresponding to the echo of each range segment. In Fig. 2, we present a schematic diagram depicting the reception of filter banks in different range segments. Suppose a radar scene contains two targets: a near, strong target denoted as target 0 and a far, weak target denoted as target 1. Obviously, if the same waveform is used in the transmitting sequence, the echo of target 1 in the second range segment will cause range ambiguity. However, with an agile waveform, different filter banks can be used to separate the echoes of different range segments to achieve range-gating. For example, filter bank 1 is used to coherently process the echo of the first range segment and then mismatch the echo of the other range segments.

However, the mismatch response between pulses cannot be ignored, and it still affects the detection and imaging of radar. Therefore, in what follows, we use the MUSIC-AP algorithm to iteratively obtain high-resolution estimation from near to far range segments. The echoes in different range segments are reconstructed to realize range ambiguity suppression.

The echo power spectrum matrix of the p th range segment can be obtained by constructing the corresponding weighted matched filter bank.

$$\mathbf{Y}_p(f, t_r) = \mathbf{R}(f) \odot \mathbf{H}_p(f) = \sum_{n=1}^P \mathbf{R}_n(f) \odot \mathbf{H}_p(f) = \mathbf{Y}_1 + \mathbf{Y}_2 \quad (50)$$

The first term of (50) is

$$\mathbf{Y}_1 = \mathbf{A}_{p, N_{spe}}(\tau) \mathbf{b}_p \mathbf{B}_{p, N_{prt}}^H(v) \quad (51)$$

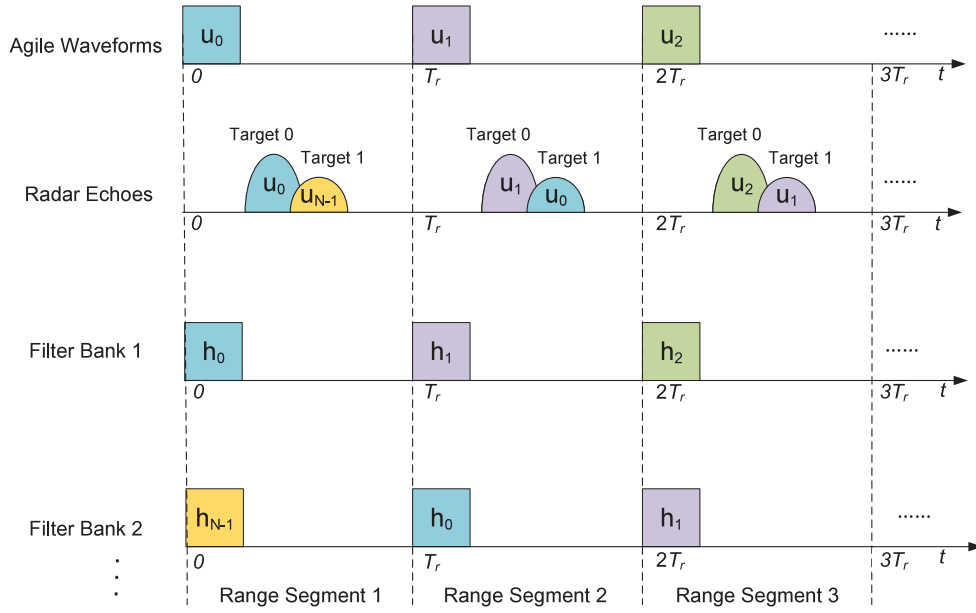


Fig. 2. Illustration of processing echoes from different range segments.

which is defined the same as that in (18). Thus, the first term Y_1 can be coherently integrated in the slow-time dimension.

The second term of (50) is

$$Y_2 = \sum_{\substack{n=1 \\ n \neq p}}^P \mathbf{A}_{n,N_{spe}}(\tau) \beta_n \mathbf{B}_{n,N_{prt}}^H(v) \odot \frac{\mathbf{U}_n(f) \odot \mathbf{U}_p(f)}{|\mathbf{U}_p(f)|^2} \quad (52)$$

For $n \neq p$, the ambiguous energy distribution on the range-Doppler plane causes Y_2 to not be coherently accumulated in the slow-time dimension. Consequently, the expected echo energy for the current range segment can be accumulated in the range-Doppler plane using the corresponding filter bank, while the ambiguous echo mismatch responses of the other range segments are dispersed on the range-Doppler plane. Performing a slow-time dimension FFT on (50) can obtain a mathematical model similar to (25).

$$S_p^*(l, v_k) = [\text{FFT}\{Y_1, t_r\}^* + \text{FFT}\{Y_2, t_r\}^*]_{v=v_k} = \sum_{k=1}^{K_{v_k}} s_{p,k} e^{j2\pi l f_{p,k}} + E_p \quad (53)$$

where $f_{p,k}$ and $s_{p,k}$ denote the range frequency and complex amplitude of the k th scatter point with Doppler frequency v_k in the p th range segment, respectively. $s_{p,k}$ includes the Doppler frequency shift phase. E_p represents the dispersed energy of the nonlocal range segment. According to the radar equation, the closer the scatterer is, the greater the energy is. Therefore, we address it according to the principle from near to far, that is, p increases from one to P . The peak data for the Doppler dimension of the current range segment can be selected by (53) for subsequent MUSIC-AP processing.

3.2. Range ambiguity suppression based on MUSIC-AP

In this subsection, we apply the MUSIC algorithm, as discussed in Section 2.2, to process the peak data obtained from the Doppler dimension, as derived in Section 3.1. However, direct echo reconstruction fails to prevent the dispersed energy effect of the second term in (50) and (53), which deteriorates the high-resolution estimate for the current range segment. Consequently, errors in target information estimation arise, leading to echo reconstruction errors and eventually reducing the ambiguity suppression performance. To address this issue, the AP scheme is employed to gradually mitigate the effect of the dispersed energy in nonlocal range segments. Finally, the MUSIC-AP

algorithm is developed to enhance the accuracy of echo reconstruction and the ambiguity suppression performance in distinct range segments.

To quantitatively evaluate the ambiguity suppression performance, we define the echo spectrum residuals for each iteration as

$$A_p^i = 20 \log_{10} \frac{\|\hat{\mathbf{R}}_p^i - \mathbf{R}_p\|_2}{\|\mathbf{R}_p\|_2} \quad (54)$$

where $\hat{\mathbf{R}}_p^i$ is the reconstruction result of the echo spectrum matrix of the p th range segment for the i th iteration and \mathbf{R}_p is the true echo spectrum matrix of the p th range segment. When noise is considered, (48) is updated as

$$\mathbf{R}(f) = \sum_{p=1}^P \mathbf{R}_p(f) + \mathbf{N}(f) \quad (55)$$

where $\mathbf{N}(f)$ is the noise term. A flow diagram of the MUSIC-AP algorithm is shown in Fig. 3.

When the number of iterations $i = 1$, the input is only the total echo spectrum minus the reconstructed echo spectrum of the first $p - 1$ nonlocal range segments.

$$\mathbf{R} - \sum_{n=1}^{p-1} \hat{\mathbf{R}}_n^i \quad (56)$$

When the number of iterations $i > 1$, the reconstructed submodule input of the p th range segment is the total echo spectrum minus the reconstructed echo spectrum of other range segments and the reconstructed noise.

$$\mathbf{R} - \sum_{n=1}^{p-1} \hat{\mathbf{R}}_n^i - \sum_{n=p+1}^P \hat{\mathbf{R}}_n^{i-1} - \hat{\mathbf{N}}^{i-1} \quad (57)$$

where $\hat{\mathbf{N}}^{i-1}$ represents the reconstructed noise at the $(i - 1)$ th iteration. The process of reconstructed submodule can be summarized as follows:

1. Weighted matched filtering is performed in the fast-time dimension of the input data for the current range segment;
2. Weighted FFT processing is performed in the slow-time dimension to obtain peak data to construct a Hankel matrix;
3. The noise subspace is obtained by singular value decomposition of the Hankel matrix;
4. By constructing the imaging function, the estimated range is obtained;

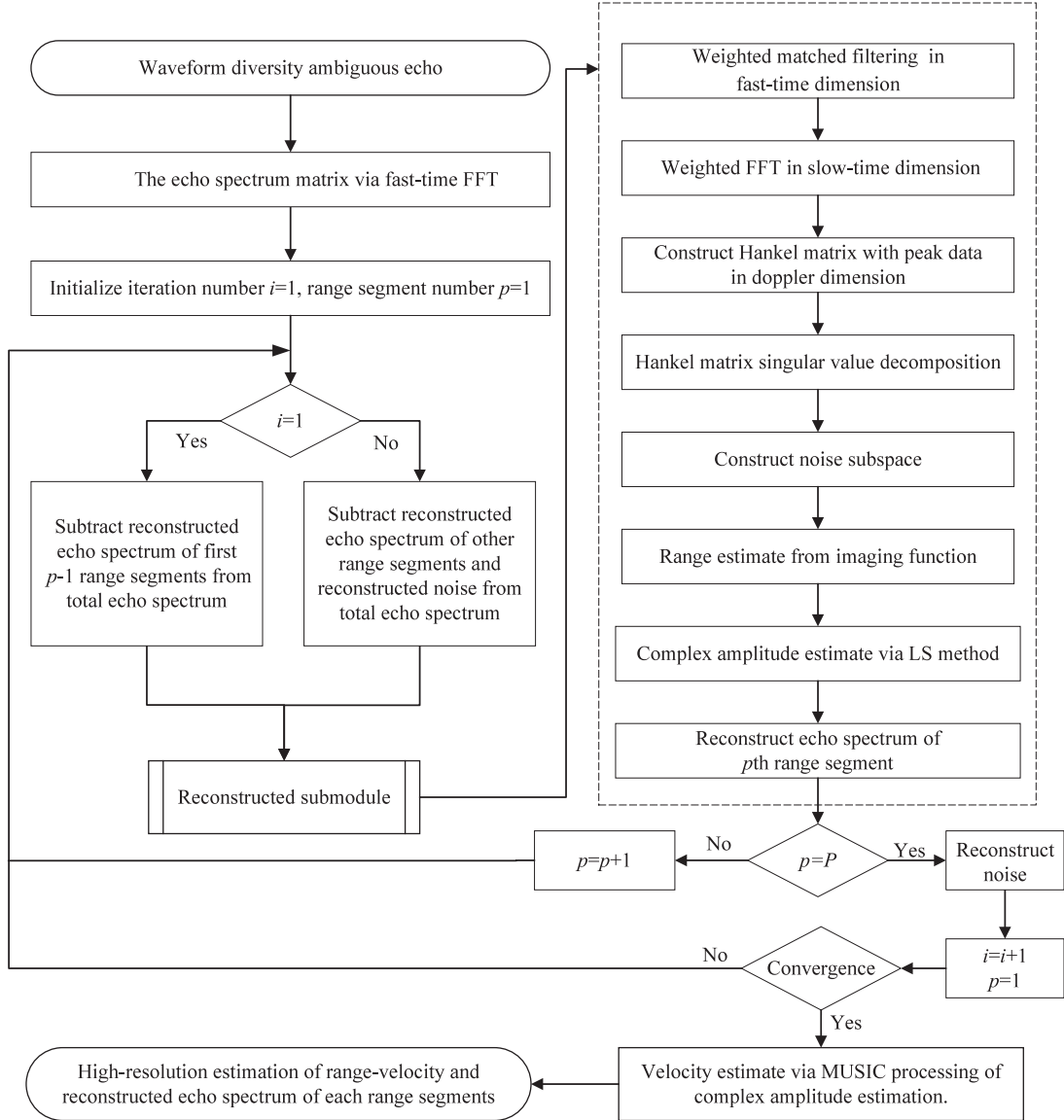


Fig. 3. Flowchart of the MUSIC-AP algorithm.

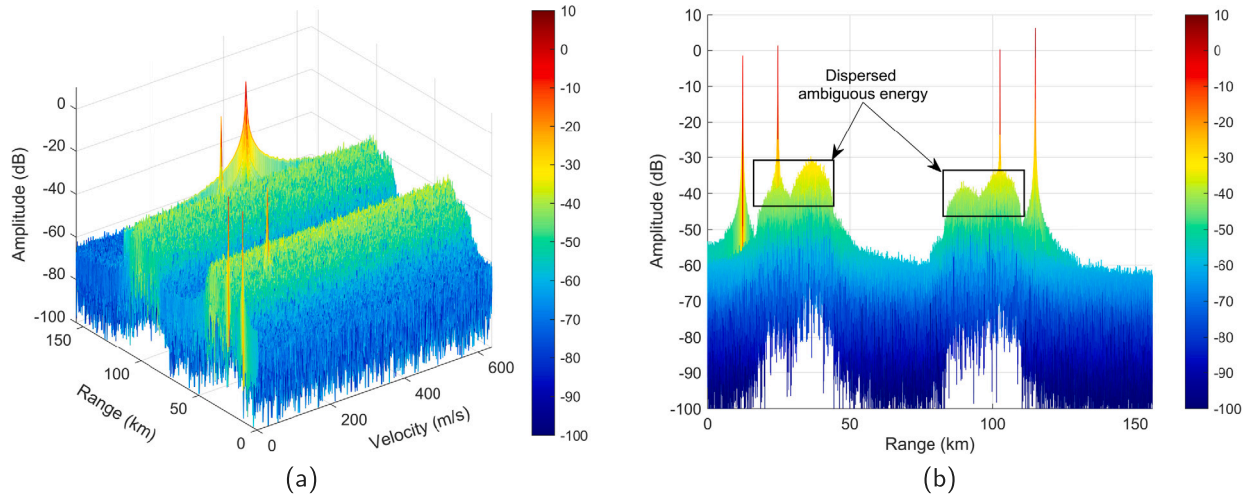


Fig. 4. (a) PD processing splicing results of the first two range segments and (b) the relevant range-amplitude projection.

5. The estimated complex amplitude is obtained through the LS method;
6. Using the above estimations and the frequency domain echo model in Section 2.1, the reconstructed echo spectrum of the p th range is obtained.

p is incremented by one. When $p = P$, an alternating projection is completed. To reconstruct the noise, $\hat{\mathbf{N}}^i = \mathbf{R} - \sum_{n=1}^P \hat{\mathbf{R}}_n^i$, set $p = 1$ and increment i by one. Then, the echo reconstruction of each range segment is repeated until the difference between the reconstructed echo spectrum of two adjacent iterations is less than the preset threshold, which is a small positive number, or reaches the maximum number of iterations. With the complex amplitude information of each range segment after convergence, including the Doppler frequency information, the velocity is estimated using the MUSIC algorithm in Section 2.2.

Ultimately, high-resolution estimation of the target's range-velocity is achieved for each range segment. The reconstructed echo spectrum of each range segment is obtained by subtracting the reconstructed echo spectrum of the nonlocal range segment and reconstructed noise from the total echo spectrum. The primary objective of this process is to enhance the algorithm's robustness and prevent poor reconstruction in a certain range segment, which will lead to the deterioration of the detection effect.

4. Simulation and performance analysis

This section provides a demonstration of the effectiveness and feasibility of the proposed algorithm through simulations, while analyzing the resolution, robustness, and sparsity of the algorithm in detail.

4.1. Point target without noise

The algorithm's high-resolution estimation and range ambiguity suppression performance is initially evaluated under an ideal scenario of a noiseless point target. The specific radar waveform parameters and target parameters are presented in Tables 2 and 3, respectively. Notably, the target range of the second range segment is the ambiguous range.

The coarse sampling range unit represents the range interval between two adjacent discrete points in the time domain echo, and the coarse sampling velocity unit represents the velocity interval between two adjacent frequency points after the FFT of the slow-time dimension echo.

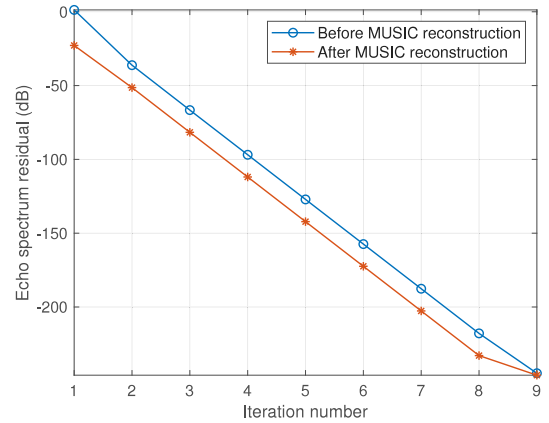


Fig. 5. Echo spectrum residual of the first range segment before and after MUSIC reconstruction. The echo spectrum before and after MUSIC reconstruction represent the input and output of the reconstruction submodule, respectively.

Table 2
Parameters of radar waveform.

Parameter	Value
Transmit waveform	Random phase-coded signal
Wavelength	0.6667 m
Number of chips	250
Chip width	0.5 μ s
Pulse width	50 μ s
Bandwidth	5 MHz
Sample frequency	5 MHz
PRT	520 μ s
Unambiguous range	78 km
Number of pulses	256
Coarse sampling range unit	30 m
Coarse sampling velocity unit	2.504 m/s

We can improve the resolution by setting the length of the imaging vector f in (34). Here we set the length of the imaging vector N_{music} to 100 000, and the length of the echo spectrum N_{spe} to 4096, and the range resolution is improved approximately 24.4-fold. The slow-time dimension echo length N_{prt} is 256, so the velocity resolution is improved approximately 390.6-fold. Then, the fine sampling range unit and fine sampling velocity unit of the algorithm are 1.2288 m and 0.00641 m/s, respectively.

Table 3
Parameters of target.

Range segment	Number	Range (m)	Velocity (m/s)
First	1	12 288	0
	2	24 576	105.0155
	3	24 588	0
	4	24 588	105
Second	5	24 576	225.2000
	6	36 864	331.2200

Assuming that there were two ambiguous range segments, the weighted matching filter was used to perform the conventional segmented PD processing on the ambiguous echo, and the range-velocity plane splicing results of the first two range segments were obtained as shown in Fig. 4. The energy of the ambiguous target in the nonlocal range segment was distributed in the range-velocity plane as the receiving filter bank mismatched the echoes from other range segments. When there are many ambiguous targets with high energy in the nonlocal range segments, the distributed energy severely affects radar target detection. Moreover, limited by the bandwidth and CPI, targets with intervals smaller than the conventional range and velocity resolution cannot be identified. As target 2 and target 4 in the first range segment cannot be distinguished, there is a target loss phenomenon.

To achieve high-resolution radar target estimation and range ambiguity suppression, the MUSIC-AP algorithm in Fig. 3 was employed. The spectrum residual of each AP and the spectrum residual curve before and after MUSIC reconstruction were obtained. The spectral residual iterative curve of the first range segment was taken as an example, as shown in Fig. 5. The reconstruction residual decreases as the number of iterations increases, and the reconstruction accuracy continues to rise, i.e., both the performance of high-resolution estimation and range ambiguity suppression are gradually improved. In the ninth iteration, the convergence condition is satisfied, and the echo spectrum residual of each range segment approaches zero; therefore, we have realized echo decorrelation and target range-velocity high-resolution estimation in different range segments.

The estimation of the target range-velocity, based on the spliced results of PD processing shown in Fig. 4, is depicted in Fig. 6(a). In the first range segment, Target 2 and Target 4 cannot be distinguished. However, after the convergence of the proposed algorithm, the range-velocity estimation of targets is displayed in Fig. 6(b). The improved range-velocity resolution ensures that no targets are lost and enables accurate high-resolution estimation of target information.

The reconstructed echo after convergence of each range segment is processed by PD, and the splicing results are shown in Fig. 7. Compared to Fig. 4, the ambiguous energy in the nonlocal range segments is

Table 4
New target parameters.

Range segment	Number	Range (m)	Velocity (m/s)
First	1	12 288	0
	2	24 576	100.01282
	3	24 578.4576	0
	4	24 578.4576	100
Second	5	24 576	200
	6	24 578.4576	200.01282

almost completely suppressed, and blind reconstruction of echoes in different range segments is achieved.

4.2. Resolution analysis

Then, the minimum range and velocity interval of the targets were set to the theoretical resolution of the algorithm, i.e., twice the fine sampling range and velocity unit, to verify the effectiveness of the algorithm in terms of improving the resolution. The parameters of the radar targets are shown in Table 4.

The spectrum residual curve of the first range segment after the MUSIC-AP algorithm processing is shown in Fig. 8. At the 12th iteration, the convergence condition is satisfied, and the spectrum residual of the echoes in each range segment approaches zero, which shows that the ideal algorithm resolution and accurate echo reconstruction can be achieved.

Similarly, as shown in Fig. 9, the two-dimensional information for the converged scattering points is spliced to obtain the result, and to accurately estimate the two-dimensional information for targets in different range segments. The range and velocity resolution reach the algorithm's theoretical resolution, and the length of the imaging vector can be independently set according to the resolution requirements. The mathematical relationship between range resolution (ΔR), velocity resolution (ΔV), and the length of the imaging vector (N_{music}) is given by the equation.

$$\Delta R = \frac{N_{spe} c}{N_{music} f_s} \quad (58)$$

$$\Delta V = \frac{\lambda}{N_{music} T_r} \quad (59)$$

where c is the signal speed, which for radar is the speed of light, and λ represents the wavelength. (58) and (59) can be used as the guideline for parameter selection.

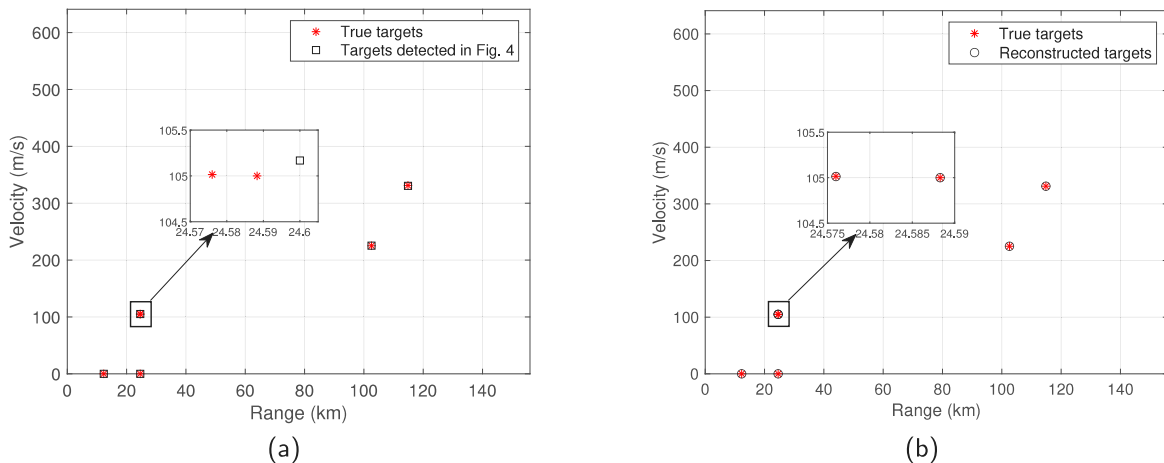


Fig. 6. Comparison of range-velocity information between the true targets and (a) targets detected in Fig. 4 and (b) reconstructed targets.

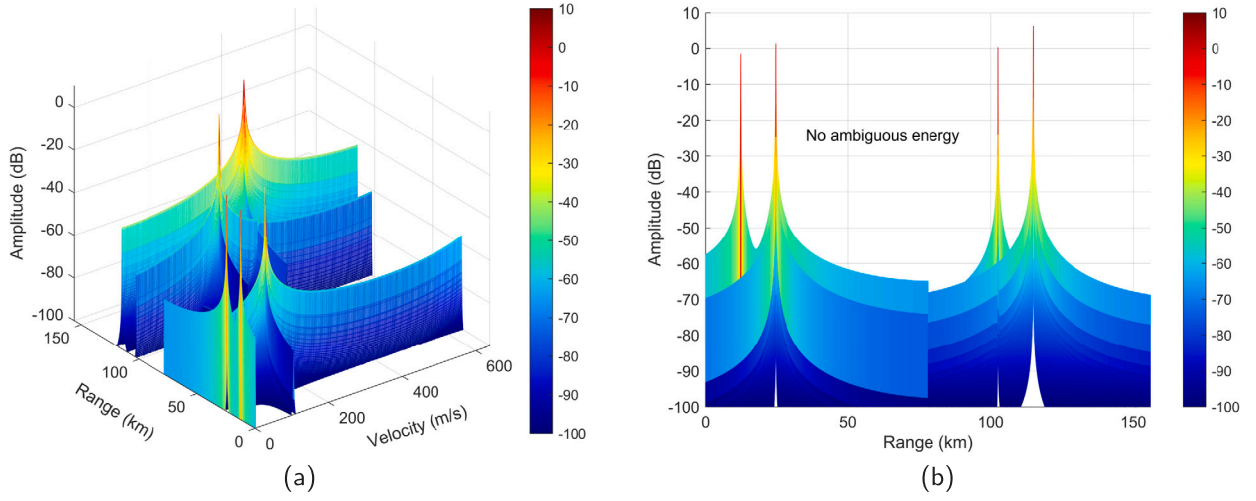


Fig. 7. (a) PD processing splicing results of the first two range segments after MUSIC-AP and (b) the relevant range-amplitude projection.

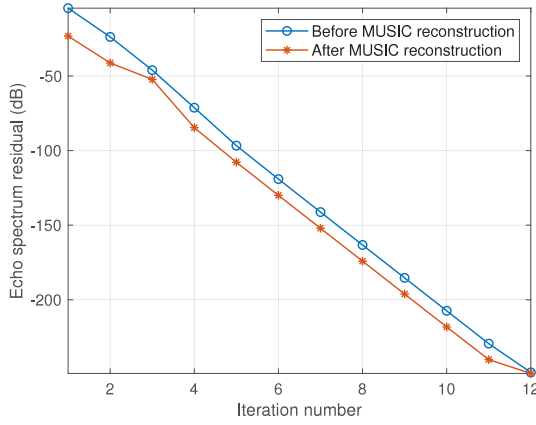


Fig. 8. Echo spectrum residual of the first range segment before and after MUSIC reconstruction when the minimum interval is the theoretical resolution.

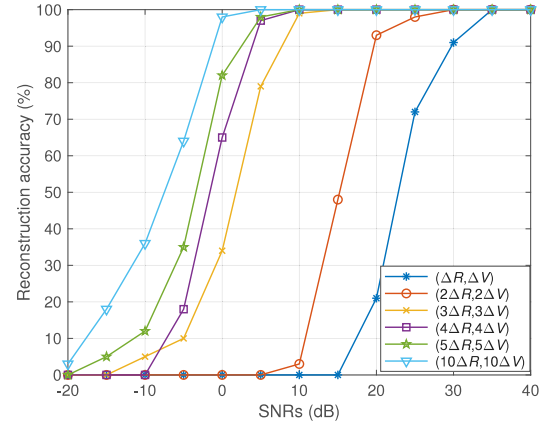


Fig. 10. Reconstruction accuracy of different target intervals under different SNRs.

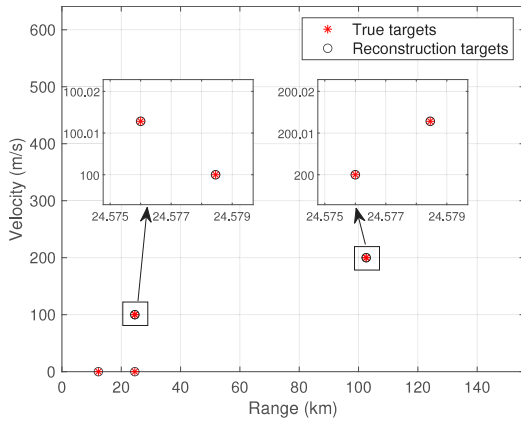


Fig. 9. Comparison of range-velocity information between true targets and reconstructed targets when the minimum interval is the theoretical resolution.

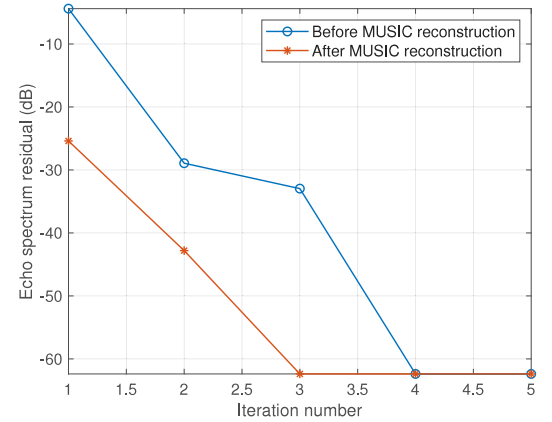


Fig. 11. Echo spectrum residual of the first range segment before and after MUSIC reconstruction in the noise scene.

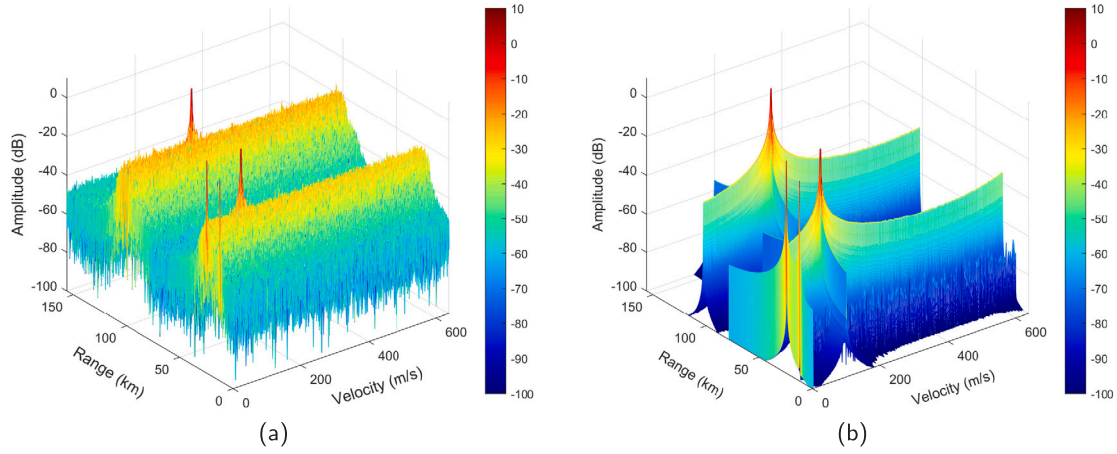


Fig. 12. Comparison between the PD results (a) before and (b) after MUSIC-AP processing in the noise scene.

4.3. Robustness analysis

Then, in a scenario with no range ambiguity, 100 Monte Carlo simulations were performed to analyze the reconstruction accuracies of different target intervals at different SNRs after matched filtering in fast and slow time. When the range and velocity estimates deviate less than a certain threshold value, the reconstruction is deemed successful. The simulation results are shown in Fig. 10.

The $(n\Delta R, n\Delta V)$ in Fig. 10 indicates that the minimum range-velocity interval of the target is n times the theoretical range-velocity resolution of the algorithm. When there is noise, the noise spatial correlation disturbance is proportional to the noise energy. Both the reconstruction accuracy and resolution are affected by a decreased SNR. The numerical simulation experiment in Fig. 10 shows that the MUSIC algorithm has high stability and low computational complexity with respect to the frequency estimation accuracy and resolution. Notably, the AP algorithm is not used here. The noise robustness of only the MUSIC algorithm is analyzed.

However, in an actual scenario, if a large amount of noise is present, it has a nonnegligible impact on the algorithm's reconstruction performance. Therefore, in the process of AP reconstruction, the impact of noise on the reconstruction accuracy can be reduced by adding a noise reconstruction subprocess. Considering the influence of noise on resolution, the parameters of the radar target were set the same as those in Table 4 except for the following:

- White Gaussian noise was added;
- The SNRs of the six targets after coherent accumulation in fast and slow time were 15, 20, 25, 30, 20 and 25;
- The minimum range interval between targets was appropriately widened to twice the theoretical range resolution, that is, the range of target 4 and target 6 was changed to 24580.9152 m, and the range of other targets remained unchanged.

The minimum velocity interval between the targets is still the theoretical velocity resolution. The objective is to verify the effectiveness of the MUSIC-AP algorithm in terms of reducing noise and to evaluate its performance in the high-resolution estimation of target parameters and range ambiguity suppression when there is noise.

The spectrum residual curve of the first range segment is shown in Fig. 11. At the fourth iteration, the convergence condition is satisfied, and the spectrum residual of the echoes in each range segment reaches approximately -60 dB, which includes the residual volumes of the ambiguous echo spectrum in nonlocal range segments and the noise spectrum. The decorrelation of the echoes in different range segments and the high-resolution estimation of radar targets are still achieved.

To verify the effect of ambiguity suppression and noise reduction, we stitched the PD results of the reconstructed echo in the first two

range segments, as shown in Fig. 12(b). Compared with Fig. 12(a), the ambiguous components are almost completely suppressed. The noise is also greatly eliminated, although it cannot be fully eliminated, and the resolution is somewhat affected. Although the resolution in the range and velocity dimensions cannot reach the theoretical resolution of the algorithm at the same time, it is still better than the Rayleigh resolution of the conventional method. The specific resolution that can be reached is associated with the residual noise volume. For details, see the Monte Carlo simulation experiment results in Fig. 10.

In conclusion, noise can affect the theoretical resolution of the algorithm. However, through our noise reconstruction subprocess, a certain degree of noise reduction can be achieved, but the noise cannot be completely eliminated. Therefore, in this simulation scenario, the range resolution interval increases to twice the theoretical range resolution interval of the algorithm, but the velocity resolution is not affected. Eventually, high-resolution estimation and range ambiguity suppression can still be achieved.

4.4. Sparsity analysis

Finally, sparsity analysis is conducted on the algorithm. As presented in Table 2, 2600 points are sampled in the range dimension in a PRT. According to the theory of the MUSIC algorithm [42], the maximum number of targets on the same velocity unit should not exceed 1300. Therefore, for the same velocity unit, different numbers of scattering points are set along the range dimension, and they are randomly distributed in the whole PRT. The minimum range interval is the theoretical range resolution of the algorithm in Section 4.2.

The simulation analysis of the sparsity requirement is shown in Fig. 13. When the number of targets increases to a certain value, target loss occurs, the estimation error increases, and the reconstructed echo spectrum residual increases. From Fig. 13(b), it can be seen that when the number of true targets is 900, all target information cannot be fully estimated. Thus, the sparsity requirement must be considered when using this algorithm.

5. Conclusion

In this paper, a novel method named MUSIC-AP is proposed for high-resolution estimation and range ambiguity suppression in PD radar. The proposed method employs waveform diversity for range-gating and transforms range-velocity estimation into spectrum estimation to make MUSIC applicable, thereby overcoming the conventional radar resolution limitation and solving the grid mismatch problem. To address the effect of ambiguous energy on reconstruction performance, the MUSIC reconstruction subprocess is embedded into the AP framework to gradually suppress the ambiguous echo energy of

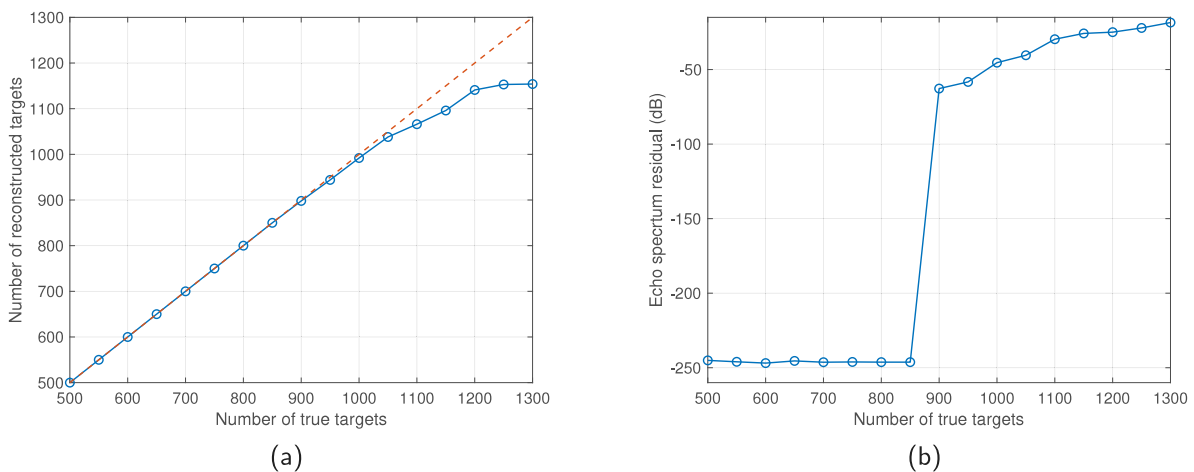


Fig. 13. The curve of (a) the number of reconstructed targets, and (b) the residual of the echo spectrum.

nonlocal range segments and noise energy, thereby improving the echo reconstruction accuracy and range ambiguity suppression performance. The high-resolution and range ambiguity suppression performance of the proposed algorithm are verified by simulations. The resolution, robustness, and sparsity of the algorithm are analyzed to provide a basis for parameter selection and scene applicability. This work offers a new perspective and iterative framework through model transformation and contributes to the field of PD radar range ambiguity suppression and imaging. Future research will focus on developing an algorithm with improved sparsity adaptation and higher computational efficiency.

CRediT authorship contribution statement

Yuanshuai Li: Conceptualization, Methodology, Software, Writing – original draft. **Shaoqiang Chang:** Data curation, Writing – original draft. **Zihao Liu:** Supervision, Writing – original draft, Validation. **Wei Ren:** Formal analysis, Writing – review & editing, Visualization. **Quant-hua Liu:** Writing – review & editing, Project administration, Funding acquisition.

Declaration of competing interest

The authors declare that they have no known competing financial interests or personal relationships that could have appeared to influence the work reported in this paper.

Data availability

The data that has been used is confidential.

References

- [1] C. Alabaster, Pulse Doppler Radar: Principles, Technology, Applications, Vol. 2, IET, 2012.
- [2] N.S. Reddy, M. Swamy, Resolution of range and doppler ambiguities in medium PRF radars in multiple-target environment, *Signal Process.* 11 (3) (1986) 223–236.
- [3] G. Trunk, S. Brockett, Range and velocity ambiguity resolution, in: The Record of the 1993 IEEE National Radar Conference, IEEE, 1993, pp. 146–149.
- [4] K. Jin, T. Lai, Y. Wang, G. Li, Y. Zhao, Radar coherent detection for Doppler-ambiguous maneuvering target based on product scaled periodic Lv's distribution, *Signal Process.* 174 (2020) 107617.
- [5] M.I. Skolnik, Introduction to Radar Systems, New York, 1980.
- [6] A. Ferrari, C. Berenguer, G. Alengrin, Doppler ambiguity resolution using multiple PRF, *IEEE Trans. Aerosp. Electron. Syst.* 33 (3) (1997) 738–751.
- [7] W. Li, W. Yi, M. Wen, D. Orlando, Multi-PRF and multi-frame track-before-detect algorithm in multiple PRF radar system, *Signal Process.* 174 (2020) 107648.
- [8] W. Li, W. Yi, L. Kong, K.C. Teh, An efficient track-before-detect for multi-prf radars with range and doppler ambiguities, *IEEE Trans. Aerosp. Electron. Syst.* 58 (5) (2022) 4083–4100.
- [9] D.P. Scholnik, Range-ambiguous clutter suppression with pulse-diverse waveforms, in: 2011 IEEE RadarCon (RADAR), IEEE, 2011, pp. 336–341.
- [10] F. Gini, A. De Maio, L. Patton, Waveform Design and Diversity for Advanced Radar Systems, Institution of Engineering and Technology, London, UK, 2012.
- [11] S.D. Blunt, E.L. Mokole, Overview of radar waveform diversity, *IEEE Aerosp. Electron. Syst. Mag.* 31 (11) (2016) 2–42.
- [12] F.-l. Lin, M. Steiner, New techniques for radar coherent range ambiguity resolution, in: Proceedings of the 2001 IEEE Radar Conference (Cat. No. 01CH37200), IEEE, 2001, pp. 99–104.
- [13] S.I. Krich, M. Montanari, V. Amendolare, P. Berestesky, Wind turbine interference mitigation using a waveform diversity radar, *IEEE Trans. Aerosp. Electron. Syst.* 53 (2) (2017) 805–815.
- [14] P. Berestesky, E.H. Attia, Sidelobe leakage reduction in random phase diversity radar using coherent CLEAN, *IEEE Trans. Aerosp. Electron. Syst.* 55 (5) (2019) 2426–2435.
- [15] Y. Bao, L. Ren, P. He, E. Mao, A novel approach for clutter cancellation in HPRF stepped-frequency radar, in: 2008 9th International Conference on Signal Processing, IEEE, 2008, pp. 2384–2387.
- [16] W.-Q. Wang, Mitigating range ambiguities in high-PRF SAR with OFDM waveform diversity, *IEEE Geosci. Remote Sens. Lett.* 10 (1) (2012) 101–105.
- [17] L. Zheng, Q. Liu, X. Wang, A. Maleki, ℓ_p -Based complex approximate message passing with application to sparse stepped frequency radar, *Signal Process.* 134 (2017) 249–260.
- [18] H. Chahrouh, S. Rajan, R. Dansereau, B. Balaji, Hybrid spread spectrum orthogonal waveforms for MIMO radar, in: 2018 IEEE Radar Conference (RadarConf18), IEEE, 2018, pp. 1010–1014.
- [19] A.C. O'Connor, Frequency-domain synthesis of advanced pulse-compression filters, in: 2019 IEEE Radar Conference (RadarConf), IEEE, 2019, pp. 1–6.
- [20] W. Baxter, E. Aboutanios, A. Hassanien, Joint radar and communications for frequency-hopped MIMO systems, *IEEE Trans. Signal Process.* 70 (2022) 729–742.
- [21] R.A. Sune, Suppressed mbiguity in range by phase-coded waveforms, in: 2001 IEEE International Geoscience and Remote Sensing Symposium, 2001, pp. 2006–2009.
- [22] D. Zhao, Y. Wei, Y. Liu, Design of unimodular sequence train with low central and recurrent autocorrelations, *IET Radar Sonar Navig.* 13 (1) (2019) 45–49.
- [23] H. Wang, Y. Zhang, J. Xu, G. Liao, C. Zeng, A novel range ambiguity resolving approach for high-resolution and wide-swath SAR imaging utilizing space-pulse phase coding, *Signal Process.* 168 (2020) 107323.
- [24] X. He, G. Liao, S. Zhu, J. Xu, J. Zhu, C. Wang, An adaptive coding-angle-Doppler clutter suppression approach with extended azimuth phase coding array, *Signal Process.* 169 (2020) 107377.
- [25] Q. Liu, W. Ren, K. Hou, T. Long, A.E. Fathy, Design of polyphase sequences with low integrated sidelobe level for radars with spectral distortion via majorization-minimization framework, *IEEE Trans. Aerosp. Electron. Syst.* 57 (6) (2021) 4110–4126.
- [26] A.C. O'Connor, J.M. Kantor, J. Jakabosky, Joint equalization filters that mitigate waveform-diversity modulation of clutter, in: 2016 IEEE Radar Conference (RadarConf), IEEE, 2016, pp. 1–6.
- [27] A.C. O'Connor, J.M. Kantor, J. Jakabosky, Filters that mitigate waveform modulation of radar clutter, *IET Radar Sonar Navig.* 11 (8) (2017) 1188–1195.
- [28] D. Zhao, N. Wang, Y. Wang, M. Zhou, Mismatched filters design to reduce range sidelobe modulation of pulse-to-pulse diverse waveform, in: 2021 CIE International Conference on Radar (Radar), IEEE, 2021, pp. 1794–1799.
- [29] M.A. Herman, T. Strohmer, High-resolution radar via compressed sensing, *IEEE Trans. Signal Process.* 57 (6) (2009) 2275–2284.

- [30] J.H. Ender, On compressive sensing applied to radar, *Signal Process.* 90 (5) (2010) 1402–1414.
- [31] Y. Yu, A.P. Petropulu, H.V. Poor, Measurement matrix design for compressive sensing-based MIMO radar, *IEEE Trans. Signal Process.* 59 (11) (2011) 5338–5352.
- [32] X. Liu, D. Cohen, T. Huang, Y. Liu, Y.C. Eldar, Unambiguous delay-doppler recovery from random phase coded pulses, *IEEE Trans. Signal Process.* 69 (2021) 4991–5004.
- [33] Y. Chi, L.L. Scharf, A. Pezeshki, A.R. Calderbank, Sensitivity to basis mismatch in compressed sensing, *IEEE Trans. Signal Process.* 59 (5) (2011) 2182–2195.
- [34] C. Wen, Y. Huang, J. Peng, J. Wu, G. Zheng, Y. Zhang, Slow-time FDA-MIMO technique with application to STAP radar, *IEEE Trans. Aerosp. Electron. Syst.* 58 (1) (2021) 74–95.
- [35] G. Tang, B.N. Bhaskar, P. Shah, B. Recht, Compressed sensing off the grid, *IEEE Trans. Inform. Theory* 59 (11) (2013) 7465–7490.
- [36] Z. Yang, L. Xie, Enhancing sparsity and resolution via reweighted atomic norm minimization, *IEEE Trans. Signal Process.* 64 (4) (2015) 995–1006.
- [37] X. He, N. Tong, X. Hu, W. Feng, Radar pulse completion and high-resolution imaging with SAs based on reweighted ANM, *IET Signal Process.* 12 (7) (2018) 868–872.
- [38] M.A. Suliman, W. Dai, Mathematical theory of atomic norm denoising in blind two-dimensional super-resolution, *IEEE Trans. Signal Process.* 69 (2021) 1681–1696.
- [39] Y. Chu, Z. Wei, Z. Yang, New reweighted atomic norm minimization approach for line spectral estimation, *Signal Process.* 206 (2023) 108897.
- [40] S. Boyd, S.P. Boyd, L. Vandenberghe, *Convex Optimization*, Cambridge University Press, 2004.
- [41] W.-k. Nie, D.-z. Feng, H. Xie, J. Li, P.-f. Xu, Improved MUSIC algorithm for high resolution angle estimation, *Signal Process.* 122 (2016) 87–92.
- [42] W. Liao, A. Fannjiang, MUSIC for single-snapshot spectral estimation: stability and super-resolution, *Appl. Comput. Harmon. Anal.* 40 (1) (2016) 33–67.
- [43] S. Boyd, J. Dattorro, *Alternating projections*, 2003, https://web.stanford.edu/class/ee392o/alt_proj.pdf.
- [44] Y. Sun, H. Fan, L. Ren, E. Mao, T. Long, Folded clutter suppression for pulse-doppler radar based on pulse-agile waveforms, *IEEE Trans. Signal Process.* 70 (2022) 3774–3788.
- [45] A. Belouchrani, K. Abed-Meraim, J.-F. Cardoso, E. Moulines, A blind source separation technique using second-order statistics, *IEEE Trans. Signal Process.* 45 (2) (1997) 434–444.